Quantification of High Temperature Stability of Mineral Wool for Fire-safe Insulation

Jensen, Peter Grouleff; Belmonte, Louise; Solvang, Mette; Yue, Yuanzheng

Published in:
Journal of Non-Crystalline Solids

DOI (link to publication from Publisher):
10.1016/j.jnoncrysol.2023.122680

Publication date:
2023

Document Version
Publisher's PDF, also known as Version of record

Journal of Non-Crystalline Solids 622 (2023) 122680

Contents lists available at ScienceDirect

Journal of Non-Crystalline Solids

journal homepage: www.elsevier.com/locate/jnoncrysol

Quantification of high temperature stability of mineral wool for fire-safe insulation

Peter G. Jensen [a], Louise Belmonte [b], Mette Solvang [b], Yuanzheng Yue [a,*]

[a] Department of Chemistry and Bioscience, Aalborg University, DK-9220 Aalborg, Denmark
[b] ROCKWOOL A/S, DK-2640 Hedehusene, Denmark

ARTICLE INFO

Keywords:
Stone wool
Glass wool
Glass
High temperature stability
Shrinkage
Crystallization

ABSTRACT

Mineral wool, particularly stone wool, is a widely applied thermal insulation material that plays a critical role both in saving energy and in slowing the spread of fire in buildings owing to its high-temperature stability (HTS). However, so far there has been a lack of a universal method to accurately quantify HTS of mineral wool on a small scale. Here, we established a universal method, which is based on measuring the variation of the silhouette area of a cylindrical wool fiber pellet during heating by a hot-stage microscope. Using this method, we detected two main stages of shrinking: 1) the first-stage shrinking related to viscous deformation; 2) the second-stage shrinking caused by melting. Minimizing the first stage shrinking is the key to ensure the fire barrier role of stone wool. The origin of the HTS differences among different types of wool products was clarified by X-ray diffraction, differential scanning calorimetry and thermal expansion.

1. Introduction

Vitreous silicate wool including mineral wool which is comprised of stone wool and glass wool [1] is a versatile material with various applications covering building insulation, industrial and technical insulation for process industry, engineered fiber solutions, noise and vibration control. Mineral wool consists of vitreous fibers with typical diameters of 2–6 μm with average lengths of around 2–6 mm [1] held together by an organic binder. Mineral wool products can be manufactured with varying densities and dimensions providing a wide range of options for customization.

Stone wool as a thermal insulation material plays a critical role in energy-saving technologies since it possesses unique advantages, such as low thermal conductivity, abundant availability of raw materials (rocks and wastes from households and industries), and easy recycling [1]. Furthermore, compared with most other wool insulators, stone wool exhibits superior high-temperature stability (HTS), i.e., the ability to maintain its original shape at elevated temperatures [1,2]. HTS of stone wool is critically important for preventing or slowing down the spread of a fire inside buildings. In this regard, stone wool can provide more time for people to escape a burning building, for firefighters to put out the fire, and thereby both lives and property can be saved.

The HTS of stone wool is a complex subject that has been investigated previously [2–14]. HTS of stone wool is controlled both by product properties (wool structure, wool slab density, and thickness) and fiber properties (e.g., chemistry, redox state of iron, fiber diameter). The fiber properties are a prerequisite for the integrity of stone wool products at elevated temperatures and are the focus of our work. The main controlling factor of HTS for stone wool fibers is the crystallization behavior, which in turn is controlled by the chemical composition e.g., by the Mg and Fe content, and the redox state of iron with a larger fraction of ferrous iron being beneficial for HTS. When stone wool fibers are heated in an oxidizing atmosphere, oxygen from the air reacts with the fiber surface oxidizing Fe^{2+} and forming nanocrystalline MgO in the process. As iron deeper in the fiber is oxidized diffusion of primarily Mg occurs toward the surface to ensure charge neutrality. This results in a progressively thicker layer of nanocrystalline MgO at the surface as the oxidation process continues. This nanocrystalline layer acts as a nucleation site and lowers the onset temperature of bulk crystallization. Furthermore, it acts as a protective shell in the viscous temperature range between the glass transition temperature and bulk crystallization. Both these effects of the Fe^{2+} improve HTS of stone wool fibers [2,4,6-9,12]. Even though the mechanism behind the HTS of stone wool fibers has been explored [2–14], the influence on fiber shrinkage has not, until now, been quantified due to the lack of a suitable method.

Within the mineral wool industry, methods such as ASTM C356 and

* Corresponding author.
E-mail address: yy@bio.aau.dk (Y. Yue).

https://doi.org/10.1016/j.jnoncrysol.2023.122680
Received 14 August 2023; Received in revised form 4 October 2023; Accepted 6 October 2023
Available online 10 October 2023

DIN 4101–17, address shrinkage behavior at elevated temperatures by comparing the dimensions of a specimen before and after heating to a specific temperature. However, none of the methods address the underlying mechanism for the wool shrinkage, since the wool deformation is strongly influenced by the product properties. Different types of wool products have different dimensions, densities, and applications. For instance, they cannot be installed identically for a construction fire test, and hence, it is hard to make a comparison in the performance of the wool materials. In other words, construction fire tests concern wool products, whereas our method presented in this work considers wool material itself. To the best of our knowledge, no construction fire test exists, which can provide a geometric parameter for comparison. But our method can lead to a comparative parameter as shown in the next section. Furthermore, construction fire tests are usually carried out under isothermal conditions, and thus, are not comparable to our dynamic heating test, where the samples undergo a heating process at a given rate.

Establishing a standard method for investigating HTS of stone wool fibers, without product properties complicating the interpretations, is important not only for the fundamental understanding of HTS but could also be a valuable tool for assessing and developing stone wool products for high-temperature applications. By using such a method, we would be capable of studying the impact of both chemical composition and processing condition (e.g., redox condition and fiber dimensions) on the high-temperature behavior of stone wool, and thereby develop the wool products with superior HTS. However, it has been difficult to set up a unified standard method for quantifying the HTS of stone wool fibers due to the following challenges. Firstly, the technique, which can visualize and detect various dynamic stages of the deformation of wool fibers, was not available. Secondly, different methods, e.g., the differential scanning calorimetry (DSC) and standard methods for quantifying HTS of stone wool products, often provide different results regarding the onset temperature of wool collapse during dynamic heating (i.e., raising the temperature at a constant heating rate). This is because the testing conditions (e.g., atmosphere, wool sample geometry, heating rate) are different. Thirdly, the mechanism of the heating-induced collapse of the wool structure is not clear, and hence it is hard to give a clear definition of HTS.

In previous studies, Scanning Electron Microscopy (SEM) imaging was used for qualitatively evaluating the change of the geometry and morphology of stone wool fibers subjected to different temperatures and atmospheres [2,5,6]. DSC was used for determining the glass transition temperature, onset temperatures of crystallization, and melting of stone wool samples [2,5,6]. However, the SEM images have limitations as they only represent a snapshot of the stone wool fibers at a single chosen temperature and do not show important events during the dynamic deformation. DSC provides no information about the geometrical stability. In contrast to the previous studies, the present work aims to establish a standard procedure for performing systematic tests of HTS on stone wool fibers using different methods. We introduce a new method, namely, hot-stage microscopy (HSM) for quantifying HTS of stone wool fiber pellets taking the effects of product properties (density and wool structure) out of the equation by keeping them fixed. The HSM data is combined with DSC and dilatometry (for determining glass transition temperature and softening point) to further clarify the causes of stone wool HTS.

HSM is a method commonly used for investigating the high-temperature behavior of different materials including vermiculite [15], glass foam [16], ceramic glaze [17,18], various vitreous fibers [19], and raw materials for stone wool production [3]. However, to the best of our knowledge, HSM has not been used for quantifying HTS of stone wool fibers. In this work, we study the geometric response of a pellet of stone wool fibers to dynamic heating with HSM. Through the geometric response of the samples to temperature, we identify several characteristic parameters, such as the onset and offset temperature of wool pellet collapse as well as the magnitude of the collapse. Then we can observe how those characteristic temperatures are affected by experimental conditions such as heating rate and fiber packing density, as well as by chemical composition of the fibers.

The characteristic temperatures measured by HSM, DSC, and dilatometry deviate from one another, and we analyze and explain the origin of this deviation. Once this has been established, we propose a universal method and parameter that can be utilized to investigate and quantify the HTS of stone wool fibers as well as other types of mineral wool. This method enables more in-depth studies of the origins of and controls on HTS of stone wool fibers and will thus contribute to the research and development of mineral wool product insulation with improved fire-protective properties.

2. Experimental

2.1. Sample preparation

Four mineral wool types were chosen as objects of this study, including three types of stone wool (SW1, SW2, and SW3) and one type of glass wool (GW). In addition, one type of alumina-silica wool (ASW) was tested. GW is known to have poor high-temperature stability (HTS), whereas ASW demonstrates exceptional HTS. Meanwhile, SW exhibits HTS levels that fall somewhere in between. These different samples were chosen to assess the applicability of the HSM method. The chemical compositions and Fe^{3+}/Fe_{tot} ($Fe_{tot}=Fe^{3+}+Fe^{2+}$) values are reported in Table 1. Wool samples were manually sieved such that a fraction of fibers with sizes of <63 μm was formed and used for both HTS and DSC measurements. Sieving the samples has three benefits: 1) breaking down the structure of the wool products; 2) removing "shots" (if any are present) which are the non-fiberized glass droplets (several millimeters in diameter); 3) providing homogenous samples, with respect to e.g., density and binder content. These three factors may also affect the HTS of wool fibers.

Another sample characteristic important for HTS is the surface area or fiber diameter. Surface crystallization is important for the HTS of stone wool fibers as described earlier, and it follows that a higher specific surface area (smaller fiber diameter) is beneficial for the HTS. The specific surface area (*SSA*) is calculated from the fiber diameter (d) of a number (n_f) of fibers measured with SEM, and fiber density (ρ). n_f for the presented results are between 800 and 2200. See Appendix 1 for derivation of the equation.

$$SSA\left[\frac{m^2}{g}\right] = \sum_{k=1}^{n_f} \frac{d_k}{\rho \times \sum_{i=1}^{n_f} (0.5 \times d_i)^2}$$

The specific surface areas for the four mineral wool samples are (in m^2/g): 0.40 (SW1), 0.28 (SW2), 0.20 (SW3), and 0.20 (GW).

2.2. HSM characterizations

For HSM characterizations, the sieved wool fibers coated with organic binder were pressed into cylindrical pellets (6.4 mm in diameter; ≈6.4 mm in height) by a hydraulic press yielding a density of around 0.9 g cm^{-3} and a porosity of around 0.7. The wool fiber pellet was placed in EM201x hot stage microscope (Hesse Instruments, Osterode, Germany), which consists of a light source, a camera, and a furnace. The camera recorded the silhouette area of the sample as a function of temperature. The cylindrical samples were heated at 10 °C/min in atmospheric air.

To see how the HSM data is affected by the density of the wool fiber pellets, we prepared fiber pellets of SW1 with varying densities (0.8 to 2.0 g/cm^3) by pressing varying amounts of sieved stone wool into pellets of the same dimensions and then measured the change of the silhouette area of the fiber pellets using HSM.

Table 1
Chemical compositions (in wt%) as measured by X-ray Fluorescence (XRF), and Fe^{3+}/Fe_{tot} (%) as measured by wet chemistry for four mineral wool samples and one ASW sample. Division of Fe into FeO and Fe_2O_3 calculated from XRF and Fe^{3+}/Fe_{tot} results. *Containing additionally estimated 6 wt% B_2O_3. The uncertainty of the measurements is given in brackets below each parameter.

Sample	SiO_2 (0.3)	Al_2O_3 (0.2)	CaO (0.1)	MgO (0.1)	Na_2O (0.1)	TiO_2 (0.1)	K_2O (<0.1)	FeO (0.2)	Fe_2O_3 (0.1)	Fe^{3+}/Fe_{tot} (5)
GW*	64	2	8	3	16	0	<1	<1	<1	NA
SW1	44	17	18	9	2	1	<1	4	3	37
SW2	40	19	16	11	2	1	1	5	4	40
SW3	41	12	30	6	1	1	<1	6	0	<3
ASW	76	24	0	0	0	0	0	NA	NA	NA

2.3. Thermal analysis and crystal identification

The DSC and thermogravimetry (TG) measurements were simultaneously carried out using a simultaneous thermal analyzer (STA) (449C Jupiter, Netzsch, Germany). Approximately 20 mg of the sieved wool fibers were placed in a Pt crucible on the sample stage next to an empty Pt crucible. To avoid sticking of the Pt crucible to the Pt stage at elevated temperatures, alumina discs were put between the crucible and the sample stage. The samples were heated from room temperature to 60 °C, held for 5 min, and subsequently heated to 1350 °C at 20 °C/min under a 50 ml/min flow of atmospheric air, and then cooled down to 200 °C at 50 °C/min, and finally to room temperature via natural cooling. Simultaneously, the mass change of the sample during heating was recorded using the TG function to monitor the chemical reactions such as binder decomposition and oxidation of ferrous to ferric ions.

The thermal expansion of a bulk glass sample with the same composition as SW1 (it should be noted that Fe^{3+}/Fe_{tot} of the bulk glass sample is 5 % as opposed to the 37 % of SW1) was measured as a function of temperature using a dilatometer (Netzsch DIL 402C, Selb/Bavaria (Germany)) at the heating rate of 2 °C/min in atmospheric air. The bulk glass sample was cut from a larger piece of glass that was collected from a production line before the melt was spun into fibers and quenched by being poured onto a brass plate. The glass was not annealed. The geometry of both the standard reference sample and the real glass samples was kept close to equal, with the sample dimensions being, 5 × 5 × 9 mm. To precisely measure the expansion of the sample, a correction was made, since the measured change in length includes both the sample holder expansion and the sample expansion. The expansion of the sample at any temperature is determined by the equation $\Delta L(T)/L_0=[L_0- L(T)]/L_0$, where L_0 and $L(T)$ are the initial length and the length at temperature T of the sample, respectively.

An important aspect of mineral wool HTS is crystallization. An aspect of the crystallization behavior that is not shown in DSC measurements is which phases that crystallize. This aspect of HTS is explored here with a focus on the stone wool samples. To obtain crystalline fibers suitable for the identification of crystalline phases, small tuffs of the individual stone wool samples were heated in a muffle furnace (K10 – Scandia Ovnen A/S) at 1000 °C for 30 min after which they were crushed in an agate mortar. XRD measurements were performed using the Panalytical Empyrean powder X-ray diffractometer (Malvern Panalytical Ltd, UK) operating at 45 kV and 40 mA, using Cu-K_α radiation. The XRD data was analyzed using HighScore Plus from Malvern Panalytical.

3. Results and discussion

The stone wool fiber sample is a compressed cylindrical wool fiber pellet, the silhouette of which can be seen in Fig. 1. As the sample is heated towards the liquidus temperature (T_L) [20] at a given rate, it undergoes two distinct stages of shrinking (see HSM curve in Fig. 1). The initial shrinkage is quantified by the ratio $\Delta A/A_0$, i.e., $(A_0\text{-}A_2)/A_0$ where A_0 and A_2 are the silhouette area at room temperature and the area at the offset of the first shrinkage, respectively. The first step of shrinkage occurs within a temperature range of ΔT = 47 °C between the onset temperature (T_1=773 °C) and the offset temperature (T_2=820 °C). A smaller $\Delta A/A_0$ indicates less shrinkage. In contrast, the second-stage shrinking takes place in a narrower temperature region of ΔT = 18 °C between the onset T_3 (1203 °C) and T_4 (1221 °C).

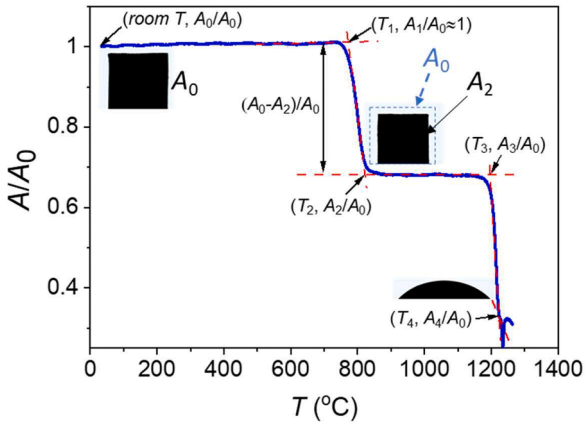

Fig. 1. The shrinking process of the cylindrical stone wool fiber pellet, reflected by the change of the black silhouette area as a function of temperature (T) (see the black images taken by the hot-stage microscope). The silhouette area is expressed as the ratio A/A_0, where A_0 and A are the initial silhouette area at room temperature and at elevated temperature T, respectively. T_1 and T_2 are the onset and offset temperatures for the first-stage shrinkage. Note that $(A_1\text{-}A_2)/A_0 \approx (A_0\text{-}A_2)/A_0$, where $A_1 \approx A_0$. T_3 is the onset temperature of the second-stage shrinkage caused by the melting of the crystallized sample. T_4 is the temperature, at which the melting process is completed, and the second-stage shrinkage is the silhouette area change normalized by A_0, i.e., $(A_3\text{-}A_4)/A_0$. Note that $A_2 \approx A_3$.

Considering the dynamic and thermodynamic behaviors of stone wool glass and melt [7], it is possible to infer the deformation mechanism of the samples during the heating process. The first-stage shrinking could be related to a gradual deformation of the wool fibers within the viscous region between T_g and T_c. In contrast, the second-stage shrinking within the narrower T region is attributed to the rapid first-order thermodynamic transition, i.e., the melting event of the crystallized wool fibers.

The first-stage shrinking is accompanied by an elastic-to-viscous transition process. That is, the elastic rigid glass state of wool fibers is transformed into the viscoelastic, but still relatively rigid state in a temperature range above the glass transition temperature (T_g), and finally into the fully viscous state at T_1, at which the sample begins to shrink. This stage of shrinking is a dynamic process that is related to a decrease in viscosity, followed by melt solidification (due to crystallization) starting at T_2. T_2 is both the offset temperature of the first shrinking and the onset temperature of the solidification of the viscous sample. The solid state survives until it starts to melt at the onset temperature (T_3) of the second collapse. Fig. 1 illustrates that A_2 is equal to A_3 in the temperature region of T_2 to T_3. To reveal the deformation mechanisms of stone wool, DSC and dilatometry measurements were performed on SW1. Details of these experiments are given in this section.

The HTS introduced in this work is a measure of the ability of the

vitreous wool to suppress its shrinking at high temperatures. In the stone wool industry, the first-stage shrinkage, which is expressed as the volume change of stone wool blocks or slabs upon heating, is often used as the main parameter of HTS to evaluate the performance of stone wool products as a fire barrier. The smaller the volume change is, the better the HTS is. However, the HTS method established by the present work yields more detailed information about the fiber stability compared to the industrial methods mentioned earlier and provides insight into the dynamics of the stone wool fiber deformation. We define the ratio A_2/A_0 as the main indicator for HTS. The $(A_3\text{-}A_4)/A_0$ value and the onset temperature (T_3) of the second collapse determine the temperature application limit for the material. However, for fire protective purposes A_2/A_0 is the most important parameter since the second-stage collapse occurs at high temperatures (>1100 °C) (for stone wool), which are generally not reached during regular construction fires, or only after very prolonged fires (ISO-834).

Before this method can be utilized to study the chemical controls on HTS it is important to understand the effects that the physical parameters, namely fiber pellet density and heating rate, of the test have on the measured HTS.

Fig. 2 shows the dependence of the HTS parameter A_2/A_0 and characteristic temperatures of SW1 on the pellet density. The results clearly demonstrate that $\Delta A/A_0$ decreases, i.e., the HTS parameter A_2/A_0 increases, with increasing sample density (Fig. 2a). This dependence is attributed to the fact that the free space available for the wool fibers to collapse into is gradually reduced by pressing the samples, i.e., with increasing the pellet density and decreasing the porosity. Furthermore, it is observed in Fig. 2b that T_1 and T_3 depend on the sample density as well. Specifically, the onset temperature (T_1) of the first stage shrinking appears to remain nearly unchanged when the density of the initial pellet density is increased from about 0.6 to 1.5 g/cm^3. But it drops by 12 °C when the density is further increased from 1.5 to 2.0 g/cm^3. This phenomenon is associated with the scenario that, when the pellet density increases, the free space inside the wool fiber pellets becomes gradually smaller, and hence the heat transfer inside the pellet becomes faster. This leads to faster heating of the fibers, and consequently to a decrease in the onset temperature of the viscous deformation. As seen in Fig. 2b, the changing trend of T_3 is comparable to that of T_1. Thus, the results in Fig. 2a and b indicate that to quantify and compare the HTS of different types of mineral wool products, it is crucial to keep the same density for the fiber pellets of different samples when preparing HTS measurements. In addition, to make the quantification of HTS more accurate, it would be appropriate to prepare the wool fiber pellets with a relatively low density, thereby allowing a larger amplitude of shrinkage ($\Delta A/A_0$) to occur in the first shrinking stage, so that we can more accurately distinguish the $\Delta A/A_0$ values of different stone wool samples.

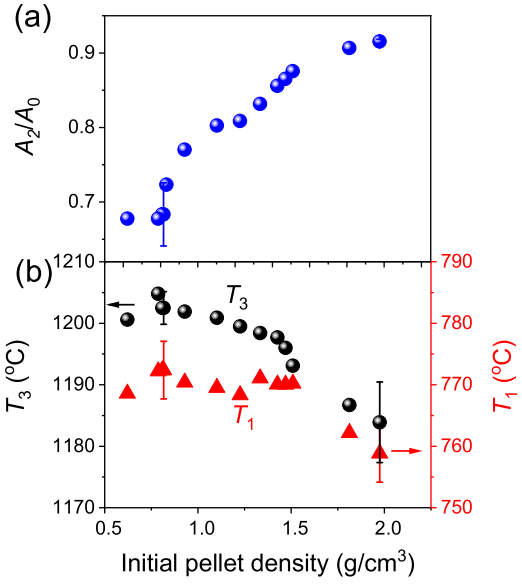

Fig. 2. Effect of the initial pellet density on both the HTS (A_2/A_0) (a), and the two characteristic temperatures, T_1 and T_3 (b) for stone wool SW1. Error bars represent 2 times the standard deviation (SD). Error bars are smaller than the symbol size for A_2/A_0 of the high-density sample.

Furthermore, we have observed in the HSM experiments that the shrinkage of the SW1 samples increases when increasing the heating rate, as shown in Fig. 3. This could be related to the situation where the fast heating means a shorter period for the sample to be oxidized and hence thinner nanocrystalline layer to form on the surface of stone wool fibers. This means that there is no sufficient nanolayer to lower the shrinking of the wool fibers. An additional experimental parameter that is important to keep in mind is the fiber diameter distribution which determines the specific surface area of the fiber sample, a factor that is important in the proportion of nanocrystalline surface layer to bulk fiber. The effect of surface area is discussed later. Now that the effects of the experimental parameters have been determined, the method can be used to obtain a deeper understanding of the origin of mineral wool HTS. To sum up, when using this method for comparing the HTS of different fibers it is important to keep the density the same (and preferably low) and the heating rate the same.

To improve the fire-protection performance of stone wool products, it is crucial to optimize both stone wool composition and product properties (density, binder content, fiber diameter, etc.). To do so, it is critically important to reveal the origin of the first stage of shrinking and to identify the key factors controlling HTS. This is done by studying the correlations of the HSM curve with the DSC output, mass change, and thermal expansion as shown in Fig. 4a and b. In the DSC and TG curves, we can observe chemical reactions, glass transition, and phase transitions in sample SW1 during dynamic heating, which are described by the following 4 steps.

Firstly, sample SW1 loses the organic binder in the temperature range from 230 to 500 °C, which is reflected by the double endotherms at 314 and 430 °C, respectively, and verified by the TG curve (Fig. 4a). *Secondly*, SW1 undergoes glass transition with the T_g of 665 °C. Meanwhile, most of the Fe^{2+} ions in SW1 fibers are oxidized to Fe^{3+} ions in the temperature region between about 450 and 800 °C, and this is confirmed by both a broad but relatively weak exothermic peak and a mass gain of 0.3 wt% due to the incorporation of oxygen into the wool fibers and formation of MgO nanolayer on the fiber surface [6]. *Thirdly*, the oxidized fibers crystallize in the range of temperature between 846 and 974 °C. *Fourthly*, the crystallized sample begins to melt at 1157 °C and becomes completely melted at 1227 °C.

The above four thermal events are helpful for explaining the area changes of the stone wool fiber pellet shown by the HSM curve in Fig. 4a

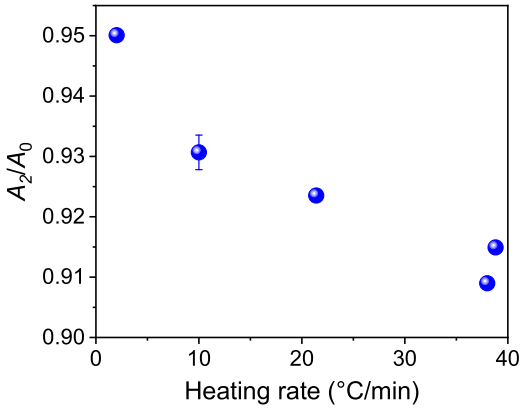

Fig. 3. Dependence of the shrinkage (A_2/A_0) on the heating rate in HSM for stone wool SW1. Error bars represent 2 times SD.

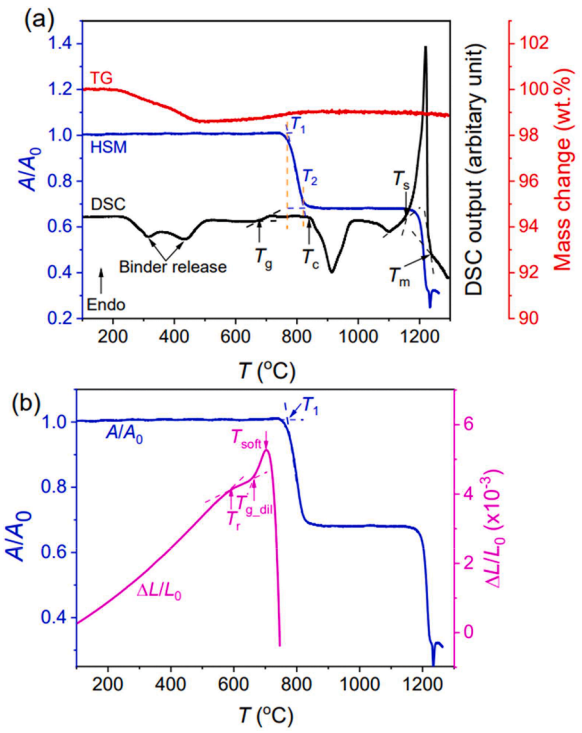

Fig. 4. (a) Comparisons between shrinkage (A/A_0), DSC output, and weight change (wt%) SW1 measured at the heating rate of 10 °C/min; (b) Comparison between the silhouette area shrinkage (A/A_0) and thermal expansion ($\Delta L/L_0$) the thermal expansion measured at a heating rate of 2 °C/min. T_g: Glass transition temperature; T_c: Crystallization onset temperature; T_s: Onset of melting; T_m: Liquidus temperature; T_1: Onset temperature of the first shrinkage stage; T_r: Relaxation temperature; T_{g_dil}: Dilatometric glass transition temperature; T_{soft}: Dilatometric softening temperature.

(and 4b), and for finding the key factor that controls the HTS of the stone wool fiber pellet. The organic binder combustion reflected by the DSC/TG causes a silhouette area increase of about 1 % in the temperature range from 230 to 500 °C (too small to be visible in Fig. 4a), as determined by HSM. The organic binder accounts for only about 1.5 wt%, and hence the expansion is small. The binder-induced expansion can in some cases be over 10 %, depending on binder content and pellet density with the effect of binder content being larger at high densities, another reason for selecting low pellet densities for HTS studies. Varying the organic binder amount leads to a variation in the degree of pellet expansion and thereby pellet densities through binder combustion. Additionally, we notice that an initial small expansion (about 1–2 %) occurs in the temperature range between room temperature and 230 °C (again not visible in Fig. 4a), which should be attributed to the expansion of air trapped in the fiber pellet.

By comparing the DSC data with the HSM data, we find that the temperature region between T_1 and T_2 in the HSM curve corresponds to the highly viscous liquid region between the T_g+82 °C and T_c-27 °C, in which the sample rapidly shrinks. When the temperature rises to 820 °C, i.e., 27 °C below the onset temperature (T_c) of bulk crystallization, the shrinking process tends to end due to surface crystallization that can be difficult to identify by DSC [2,6]. When temperature increases to T_c, bulk crystallization starts, thereby causing a complete termination of the viscous deformation, leading to the end of shrinking. Then, A/A_0 remains constant before the temperature rises to T_3 (Fig. 1), i.e., the onset temperature of the second-stage shrinking, which corresponds to the onset temperature (T_S) of the melting process of the crystallized wool (Fig. 4a). The second-stage shrinking ends at the melting point (T_m) as shown by the DSC curve in Fig. 4a.

Fig. 4b shows the comparison between the HSM curve and the thermal expansion curve for a bulk glass with a composition corresponding to SW1, which can also give insight into the origin of the wool fiber shrinking. The dilatometric softening point (T_{soft}) and the dilatometric glass transition temperature (T_{g_dil}) for the bulk glass piece with the same composition as SW1 are 703 °C and 665 °C, respectively, at the heating rate of 2 °C/min. The bulk glass sample demonstrates softening at a temperature of 703 °C (T_{soft}), while the wool fiber pellet undergoes significant shrinkage starting at 747 °C (T_1). The cause of shrinkage processes is viscous deformation, meaning the end of the viscoelastic deformation. We attribute the 44 °C difference between T_{soft} and T_1 to the following two reasons. Firstly, the bulk sample undergoes the heating process under a mechanical load (0.5 N), and thus this load allows the bulk glass sample to deform at a lower temperature compared to the wool fiber pellet that undergoes heating under no load. Secondly, the crystalline nanolayer (primarily consisting of MgO) exists on the surface of stone wool fibers, and it shifts the viscous deformation event to higher temperatures compared to the deformation temperature of the bulk sample as wool fibers possess a significantly larger specific surface area, and hence, a significantly larger amount of the nanocrystalline layer. In other words, if there were no sufficient nanocrystalline layer, wool fibers would shrink at a temperature closer to the bulk sample. Moreover, the nanolayer enables the primary bulk crystallization to occur at lower temperatures, thereby reducing the degree of shrinking.

In addition, the thermal expansion curve in Fig. 4b shows a decelerating stage of expansion in the temperature range between T_r (588 °C) and T_{g_dil} (663 °C). This phenomenon is attributed to the volume relaxation below the glass transition temperature that occurs in a rapidly cooled glass. The glass sample used for the dilatometric measurement was not subjected to annealing after the process of melt-quenching. A rapidly cooled glass has a larger free volume and a higher enthalpy compared to a slowly cooled or annealed glass [21].

As depicted in Fig. 1, the A_2/A_0 value serves as a quantitative indicator of the wool fiber HTS with the effects of product properties such as density, and wool structure eliminated. Having a general understanding of the mechanisms behind the shrinkage behavior of mineral wool fibers and the observations made with the HSM we wish to assess the applicability of the HTS quantification method. We do that by measuring the HTS of several different types of wool fiber. The fiber types are: One type of glass wool (GW), three types of stone wool (SW1–3), and one type of alumina-silica wool (ASW). We have selected these fiber types because GW is known to have a low HTS, ASW an extremely high HTS and SW falls somewhere in between the two other types in terms of HTS. For the HTS quantification method to be meaningful it is important that the method can clearly show these well-known differences between fiber types. Furthermore, three distinct types of SW have been selected to conduct a more detailed investigation into the origin of HTS for SW specifically.

As is seen in Fig. 5a and Table 2, the onset temperature (T_1) of the first-stage shrinking varies in the order of GW < SW1 < SW2 < SW3 < ASW, while the onset temperature (T_3) of the second-stage shrinking varies in the order: GW < SW3 < SW2 ≈ SW1 < ASW. The HTS value (A_2/A_0) increases in the sequence of GW< SW1 < SW2 < SW3 < ASW. Clearly, ASW possesses the highest HTS among the five wool products as it does not shrink at all in the investigated temperature range (up to 1260 °C). This is because ASW has a strong tendency to crystallize, i.e., it crystalizes even prior to the completion of glass transition [22,23] and does not undergo any viscous deformation before the maximum scanning temperature in the HSM. Upon an overall assessment, ASW is the best fire barrier since it exhibits not only the highest A_2/A_0 value (≈1) but also the highest T_3 and T_m values. We included ASW in this study for two reasons. Firstly, we aimed to validate the effectiveness of our approach in ranking the HTS of diversified wool products. Secondly, we sought to investigate the underlying reasons for the variation in HTS among different fiber types, utilizing the significant crystallization tendency of ASW.

Fig. 5 and Table 2 show that the HSM method clearly demonstrates

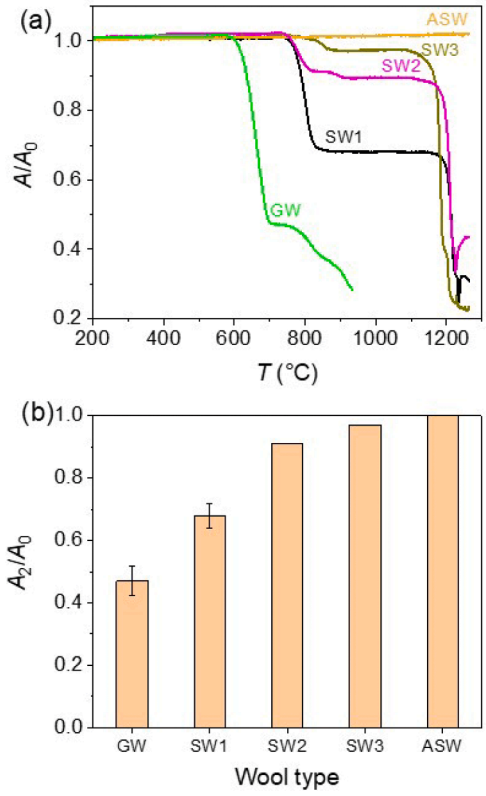

Fig. 5. Quantification of high-temperature stability of different types of vitreous wool for thermal insulation by means of HSM. (a): The shrinkages (A/A_0) of glass wool (GW), stone wool (SW1, SW2, and SW3), and alumina silicate wool (ASW) upon dynamic heating. (b): The HTS parameter (A_2/A_0) for the different wool products. Error bars represent 2 times SD.

the expected differences in HTS between GW, SW, and ASW. This difference is easy to explain when comparing their crystallization behaviors [1,22,23]. That is, the glass wool does not crystallize during heating, instead, it behaves as a viscous melt above T_g, and hence, rapidly shrinks with increasing temperature. In contrast, the stone wool fibers crystallize during heating, thereby suppressing the first stage shrinking to various extent, depending on its chemical composition. By comparing different types of stone wool fibers, we can detect striking differences in their HTS (A_2/A_0). In Fig. 5a and b, it is interesting to see a large difference in HTS, i.e., A_2/A_0 between SW1 and SW2, despite only small differences in chemical composition and iron redox state between the two samples (Table 1). According to the chemical analyses, SW2 possesses 2 wt% less CaO, and 2 wt% more MgO than SW1. Furthermore, SW2 has 1 wt% more FeO than SW1 meaning that more Fe^{2+} ions are available for oxidation in SW1. As a result, more alkaline earth ions can diffuse to the fiber surface of SW2 compared to SW1 [6]. Consequently, after the heating process, SW2 must have a thicker oxidation-induced nanocrystalline layer than SW1. This nanocrystalline layer difference could be one of the main causes of the difference in the crystallization and shrinkage behavior between SW1 and SW2.

In Fig. 5a and b, another striking scenario is observed where SW3 features the highest HTS (A_2/A_0=0.97) among the three stone wool samples. By studying the DSC and XRD results (Fig. 6a and b) the origin of the high HTS of SW3 can be deduced. In contrast to the other two stone wool samples, the DSC upscan curve of SW3 shows a broad but shallow exothermic peak between T_g and T_c, i.e., in the temperature region of viscous deformation. The broad exothermic peak of the DSC curve can be explained as follows. SW3 contains 6 wt% FeO and ≈0 % Fe_2O_3 i.e., all the iron exists in the ferrous state. When SW3 is heated in HSM and DSC in atmospheric air, Fe^{2+} reacts with oxygen, yielding Fe^{3+} and forming a nanocrystalline MgO layer in the process [6]. Both the oxidation of ferrous iron and the nanocrystal formation cause the release of the internal energy of SW3 fibers, thereby leading to the broad exothermic peak prior to the primary crystallization event. Such a broad DSC peak is not detectable in the other two samples since their Fe^{2+} content is lower (FeO=4 wt% (SW1) and FeO=5 wt% (SW2)) than that of SW3 (6 wt%). Although the absolute differences in FeO content between the three samples are relatively small, the relative differences in FeO are significantly larger, e.g., SW3 and SW2 have 50 wt% and 20 wt % more FeO than SW1.

The nanolayer on the surface of wool fibers is composed of MgO and CaO, and this hard crystalline *skin* limits the viscous deformation i.e., shrinking [6]. Subsequently to the surface crystallization, the bulk crystallization takes place between the onset (about 870 °C) and the offset temperature (990 °C) of the bulk crystallization (Fig. 6). An interesting observation is the inverse correlation between fiber surface area and HTS (A_2/A_0) for the three stone wool fibers, where the surface areas as mentioned earlier are (in m^2/g): 0.40 (SW1), 0.28 (SW2), 0.20 (SW3). Surface area is an important control of crystallization and could be important for HTS as discussed earlier. However, our results indicate that, within the range present for the selected stone wool fibers, surface area is of secondary importance.

To further understand the crystallization behavior of the stone wool fibers, XRD measurements were performed on the three samples that were treated at 1000 °C for 30 min. As seen in Fig. 6b, the three thermally treated samples have different crystalline phases. In detail, after heat treatment, both SW1, SW2, and SW3 contain augite, and SW3 contains akermanite in addition to the augite. The formation of akermanite ($2CaO\text{-}MgO\text{-}2SiO_2$) could be attributed to the much larger amount of CaO (about 30 wt%) in SW3 compared to the other two types of samples. The XRD measurements show that the identity of the crystalline phases is not necessarily the main control on HTS since SW1 and SW2 are shown to have almost the same crystalline content whereas their HTS is significantly different.

4. Conclusions

We established a facile and effective standard method to quantify the high-temperature stability (HTS) of mineral wool fibers. The method is based on the hot-stage microscope (HSM) in which a wool fiber pellet is dynamically heated at 10 °C/min, and the heating-induced change of the silhouette area of the pellet can be determined. We showed that stone wool goes through two stages of shrinking in different temperature

Table 2
Characteristic values for the four mineral wool products and the one ASW product collected from Figs. 5a, 6a, and [23]. DSC upscan rate was 20 K/min and HSM upscan rate was 10 K/min. Standard deviations for HSM are presented in brackets. The uncertainties of T_g and T_m values are ±1 °C [24] and ±4 °C [25], respectively. The uncertainties of T_c and T_p lie between those of T_g and T_m.

Wool	T_1 (°C)	T_2 (°C)	T_3 (°C)	T_4 (°C)	A_2/A_0	T_g (°C)	T_c (°C)	T_p (°C)	T_m (°C)
GW	623(0.9)	692(1.0)	776(1.5)	NA	0.47(0.02)	NA	NA	NA	NA
SW1	773(2.3)	820(0.7)	1203(1.3)	1221	0.68(0.02)	677	861	927	1231
SW2	751	817	1197	1216	0.91	666	884	924	1213
SW3	811	869	1172	1188	0.97	687	873	934	1207
ASW	NA	NA	NA	NA	1.00	891	965	979	NA

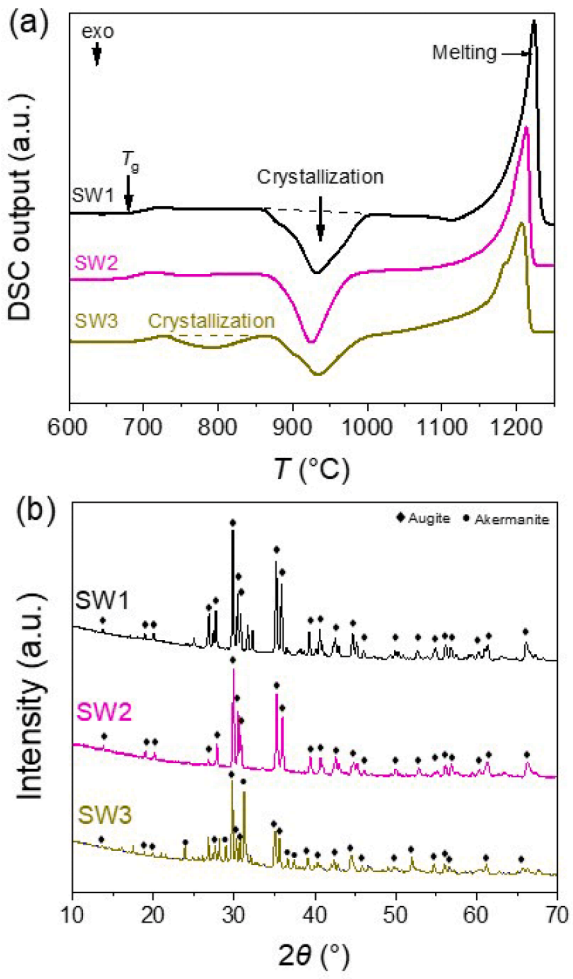

Fig. 6. (a) DSC upscans for stone wool samples SW1, SW2, and SW3 (b) XRD patterns of the three stone wool samples, all of which were subjected to isothermal treatment at 1000 °C for 30 min in atmospheric air.

regions during heating. We showed that it is important to control the density of the wool pellets as it affects both the amount of shrinkage as well as T_1 and T_2. We suggest using a low-density wool pellet (around 1 g/cm^3) to obtain a wide range of possible degrees of shrinkage as well as limit the effect of the organic binder. The first stage of shrinking is attributed to the viscous deformation of the glass phase, while the second stage is the result of the melting of the crystallized fibers. In contrast, glass wool undergoes only one continuous shrinking due to the viscous flow which fits with observations from literature showing that it does not crystallize during heating at the selected heating rates.

The first-stage shrinkage was found to be a key value for evaluating the high-temperature stability of wool as it is sensitive to the fiber composition and the redox state of iron. Thus, the ratio A_2/A_0., where A_0 and A_2 are the silhouette areas of the wool fiber pellet at room temperature and after the first-stage shrinking, respectively, was defined as the main indicator for HTS. Using this ratio, we ranked the high-temperature stability for four mineral wools, one glass wool sample, three stone wool samples, and one alumina-silica glass wool. To compare the HTS of different types of mineral wool fibers, besides A_2/A_0, the onset temperatures (T_1 and T_3) for both the first-stage shrinking and the second-stage shrinking (melting) should be used as well. T_3 determines the upper-temperature application limit of the mineral wool, given that A_2/A_0 is sufficiently low.

CRediT authorship contribution statement

Peter G. Jensen: Conceptualization, Methodology, Validation, Formal analysis, Investigation, Writing – original draft, Writing – review & editing, Visualization. **Louise Belmonte:** Conceptualization, Resources, Writing – review & editing, Funding acquisition. **Mette Solvang:** Conceptualization, Writing – review & editing. **Yuanzheng Yue:** Conceptualization, Methodology, Writing – original draft, Writing – review & editing, Visualization, Supervision.

Declaration of Competing Interest

The authors declare that they have no known competing financial interests or personal relationships that could have appeared to influence the work reported in this paper.

Data availability

Data will be made available on request.

Acknowledgments

This work was financially supported by ROCKWOOL A/S.

Appendix 1: Derivation of equation for calculation of specific surface area of mineral wool

The derivation of an equation for calculating the specific surface area of a mineral wool sample based on fiber diameter measurements is based on the following three assumptions:

1 The fibers are shaped like rods with constant diameters along the fibers. The area of the rod ends is not included in the calculations.
2 The lengths of the fibers are independent of fiber diameter.
3 The specific surface area for the sample is calculated as a mass-weighted sum of the specific surface area of each individual fiber.

The specific surface area (A) of a single measured fiber with density ρ, radius r, diameter d, and length L is calculated as follows:

$$A\left[\frac{m^2}{g}\right] = \frac{2 \times r \times \pi \times L}{\rho \times r^2 \times \pi \times L} = \frac{2}{\rho \times r} = \frac{4}{\rho \times d}$$

The mass fraction (f) of a single fiber is calculated as the ratio of the mass of the individual fiber to the combined mass of all in all n_f (number of measured fibers) measured fibers:

$$f = \frac{(0.5 \times d)^2 \times \pi \times \rho}{\sum_{i=1}^{n_f}(0.5 \times d_i)^2 \times \pi \times \rho} = \frac{(0.5 \times d_i)^2}{\sum_{i=1}^{n_f}(0.5 \times d_i)^2}$$

The specific surface area (SSA) of all n_f measured fibers is calculated as a weighted sum of the individual fibers' specific surface areas:

$$SSA\left[\frac{m^2}{g}\right] = \sum_{k=1}^{n_f}(A_k \times f_k) = \sum_{k=1}^{n_f}\left(\frac{4}{\rho \times d_k} \times \frac{(0.5 \times d_k)^2}{\sum_{i=1}^{n_f}(0.5 \times d_i)^2}\right)$$

$$SSA\left[\frac{m^2}{g}\right] = \sum_{k=1}^{n_f} \frac{d_k}{\rho \times \sum_{i=1}^{n_f}(0.5 \times d_i)^2}$$

References

[1] Y.Z. Yue, M. Solvang, Stone and glass wool, in: P. Richet (Ed.), Encyclopedia of Glass Science, Technology, History, and Culture, John Wiley and Sons, Inc., Hoboken, New Jersey, 2021, pp. 1103–1112, vol. II.

[2] M.M. Smedskjaer, M. Solvang, Y. Yue, Crystallisation behaviour and high-temperature stability of stone wool fibres, J. Eur. Ceram. Soc. 30 (2010) 1287–1295.

[3] V. Schultz-Falk, K. Agersted, P.A. Jensen, M. Solvang, Melting behaviour of raw materials and recycled stone wool waste, J. Non-Cryst. Solid. 485 (2018) 34–41.

[4] E.R. Nielsen, M. Augustesen, K. Ståhl, Devitrification and high temperature properties of mineral wool, Mater. Sci. Forum 558-559 (2007) 1255–1260.

[5] D. Xing, C. Chang, X.Y. Xi, B. Hao, Q. Zheng, S.I. Gutnikov, B.I. Lazoryak, P.C. Ma, Morphologies and mechanical properties of basalt fibre processed at elevated temperature, J. Non-Cryst. Solid. 485 582 (2022), 121439.

[6] Y. Yue, M. Korsgaard, L.F. Kirkegaard, G. Heide, Formation of a nanocrystalline layer on the surface of stone wool fibers, J. Am. Ceram. Soc. 92 (2009) 62–67.

[7] M. Moesgaard, H.D. Pedersen, Y.Z. Yue, E.R. Nielsen, Crystallization in stone wool fibres, J. Non-Cryst. Solid. 353 (2007) 1101–1108.

[8] R.F. Cooper, J.B. Fanselow, D.B. Poker, The mechanism of oxidation of a basaltic glass: chemical diffusion of network-modifying cations, Geochim. Cosmochim. Acta. 60 (1996) 3253–3265.

[9] P.M. Sørensen, M. Pind, Y.Z. Yue, R.D. Rawlings, A.R. Boccaccini, E.R. Nielsen, Effect of the redox state and concentration of iron on the crystallization behavior of iron-rich aluminosilicate glasses, J. Non-Cryst. Solid. 351 (2005) 1246–1253.

[10] S.I. Gutnikov, M.S. Manylov, B.I. Lazoryak, Crystallization and thermal stability of the p-doped basaltic glass fibers, Minerals 9 (2019) 615.

[11] S.I. Gutnikov, M.S. Manylov, Y.v. Lipatov, B.I. Lazoryak, K.v. Pokholok, Effect of the reduction treatment on the basalt continuous fiber crystallization properties, J. Non-Cryst. Solid. 368 (2013) 45–50.

[12] M.M. Smedskjaer, Y.Z. Yue, J. Deubener, S. Mørup, Impact of cationic diffusion on properties of ironbearing glass fibres, Phys. Chem. Glasses: Eur. J. Glass Sci. Technol. B 51 (2010) 271–280.

[13] L. Luo, Q. Zhang, Q. Wang, J. Xiao, J. Liu, L. Ding, W. Jiang, Effect of the iron reduction index on the mechanical and chemical properties of continuous basalt fiber, Mater. (Basel) 12 (2019) 2472.

[14] M.P. Krasnovskih, N.G. Maksimovich, Y.I. Vaisman, A.A. Ketov, Thermal stability of mineral-wool heat-insulating materials, Russ. J. Appl. Chem. 87 (2014) 1430–1434.

[15] R.R. Petersen, J.F.S. Christensen, N.T. Jørgensen, S. Gustafson, L.A. Lindbjerg, Y. Yue, Preparation and thermal properties of commercial vermiculite bonded with potassium silicate, Thermochim. Acta. 699 (2021), 178926.

[16] R.R. Petersen, J. König, Y. Yue, Evaluation of foaming behavior of glass melts by high-temperature microscopy, Int. J. Appl. Glass Sci. 7 (2016) 524–531.

[17] F.M. Stábile, M. Piccico, M.F. Serra, M. Rafti, G. Súarez, N.M. Rendtorff, Viscosity and thermal evolution of density and wetting angle of a commercial glaze by means of hot stage microscopy, Procedia Mater. Sci. 9 (2015) 563–570.

[18] M.G. Rasteiro, T. Gassman, R. Santos, E. Antunes, Crystalline phase characterization of glass-ceramic glazes, Ceram. Int. 33 (2007) 345–354.

[19] A.F. Gualtieri, E. Foresti, I.G. Lesci, N. Roveri, M.L. Gualtieri, M. Dondi, M. Zapparoli, The thermal transformation of Man Made Vitreous Fibers (MMVF) and safe recycling as secondary raw materials (SRM), J. Hazard. Mater. 162 (2009) 1494–1506.

[20] Y.Z. Yue, Q.J. Zheng, Fiber spinnability of glass melts, Int. J Appl. Glass Sci. 8 (2017) 37–47.

[21] Q. Zheng, Y. Zhang, M. Montazerian, O. Gulbiten, J.C. Mauro, E.D. Zanotto, Y. Z. Yue, Understanding glass through differential scanning calorimetry, Chem. Rev. 113 (2019) 7848–7939.

[22] Y.Z. Yue, C.A. Angell, Clarifying the glass-transition behavior of water by comparison with hyperquenched inorganic glasses, Nature 427 (2004) 717–720.

[23] Y.F. Zhang, L.N. Hu, S.J. Liu, C.F. Zhu, Y.Z. Yue, Sub-Tg enthalpy relaxation in an extremely unstable oxide glass and its implication for structural heterogeneity, J. Non-Cryst. Solid. 381 (2013) 23–28.

[24] Y. Yue, Characteristic temperatures of enthalpy relaxation in glass, J. Non-Cryst. Solid. 354 (2008) 1112–1118.

[25] Q. Zheng, J. Zheng, M. Solvang, Y. Yue, J.C. Mauro, Determining the liquidus viscosity of glass-forming liquids through differential scanning calorimetry, J. Am. Ceram. Soc. 103 (2020) 6070–6074.